T 1D -weighted ihMT imaging – Part I. Isolation of long- and short-T 1D components by T 1D -filtering

Andreea Hertanu, Lucas Soustelle, Arnaud Le Troter, Julie Buron, Julie Le Priellec, Victor N D Carvalho, Myriam Cayre, Pascale Durbec, Gopal Varma, David C Alsop, et al.

T_{1D}-weighted ihMT imaging – Part I. Isolation of long and short T_{1D} components by T_{1D}-filtering

Andreea Hertanu[1,2], Lucas Soustelle[1,2], Arnaud Le Troter[1,2], Julie Buron[1,2,3], Julie Le Priellec[3], Victor N.D. Carvalho[1,2,4], Myriam Cayre[3], Pascale Durbec[3], Gopal Varma[5], David C. Alsop[5], Olivier M. Girard[1,2], Guillaume Duhamel[1,2]*

1. Aix Marseille Univ, CNRS, CRMBM, Marseille, France
2. APHM, Hôpital Universitaire Timone, CEMEREM, Marseille, France
3. Aix Marseille Univ, CNRS, IBDM, Marseille, France
4. Aix Marseille Univ, CNRS, ICR, Marseille, France
5. Division of MR Research, Radiology, Beth Israel Deaconess Medical Center, Harvard Medical School, Boston, MA, United States

*Corresponding author:

Guillaume Duhamel

Centre de Résonance Magnétique Biologique et Médicale

Aix Marseille University, CNRS UMR 7339

13005 Marseille, France

guillaume.duhamel@univ-amu.fr

+33 491 386 260

ABSTRACT (word count: 199)

Purpose: To identify T_{1D} filtering methods, which can specifically isolate various ranges of T_{1D} components as they may be sensitive to different microstructural properties.

Methods: Modified Bloch-Provotorov equations describing a bi-T_{1D} component biophysical model were used to simulate the ihMT signal from ihMTRAGE sequences at high RF power and low duty-cycle with different switching time values for the dual saturation experiment: Δt = 0.0, 0.8, 1.6, 3.2 ms. Simulations were compared with experimental signals on the brain grey and white matter tissues of healthy mice at 7T.

Results: The lengthening of Δt created ihMT high-pass T_{1D}-filters, which efficiently eliminated the signal from T_{1D} components shorter than 1 ms, while partially attenuating that of longer components (≥ 1 ms). Subtraction of ihMTR images obtained with Δt = 0.0 ms and Δt = 0.8 ms generated a new ihMT bandpass T_{1D}-filter isolating short T_{1D} components in the 100 µs to 1 ms range. Simulated ihMTRs in CNS tissues were confirmed experimentally.

Conclusion: Long and short T_{1D} components were successfully isolated with high RF power and low duty-cycle ihMT filters in the healthy mouse brain. Future studies should enable the investigation of the various T_{1D} ranges microstructural correlations in in vivo tissues.

Keywords: ihMT T_{1D}-filtering, high-passT_{1D}-filter, bandpass T_{1D}-filter, low duty-cycle, bi-T_{1D} model

Running title: Isolation of long and short T_{1D} components by ihMT T_{1D}-filtering

Body text word count: 5346 words

INTRODUCTION

Inhomogeneous magnetization transfer (ihMT) is an MRI technique (1), weighted by $T_{1D,}$ the dipolar order relaxation time (2), an endogenous source of contrast driven by slow molecular dynamics and tissue microstructure (3,4).

An increasing number of ihMT studies have focused on Central Nervous System (CNS) applications (1,2,5–25), more specifically myelin imaging. Indeed, due to its highly organized multi-layered stack ultrastructure (26), myelin represents a suitable candidate for ihMT imaging. Molecular motions in myelin are limited and thus generate anisotropic dynamics and unaveraged dipolar interactions (27) that lead to dipolar order, detected in an ihMT experiment through the difference between single- and dual- offset frequency saturation MT images (1).

The T_{1D} weighting of the ihMT signal was previously shown to be adjustable through Δt, the switching time between the application of RF pulses at positive and negative offset frequencies in the dual saturation (10). Frequency-alternating pulses with incremental Δt values can thus be used to eliminate the signal contribution from components with increasing values of T_{1D}.

Such strategy, called T_{1D}-filtering, allowed contrast optimization between long T_{1D} CNS structures and short T_{1D} muscle tissue (10) and touched upon a relationship between the strength of the T_{1D}-filtering (i.e., value of Δt) and the specificity of ihMT to CNS myelin (17). However, the pulse length and therefore the pulse power were not kept

constant for all investigated Δts in either of the two studies, thereby making any variation of the ihMT signal the mixed result of power (28) and switching time effects.

A modified version of the ihMT sequence (8) in which the pulse power could be kept constant independent of the values of Δt, allowed quantification of T_{1D} using an advanced biophysical model derived from the modified Bloch-Provotorov equations (8,10). A recent study extended this model by including multiple dipolar compartments and showed the ihMT signal decay is more accurately characterized by a minimum of two non-null T_{1D} components, including a sub-millisecond component, provided a suitably high RF power is used for off-resonance saturation (18).

Generally speaking, approaches using high RF power for saturation are necessary for Signal-to-Noise Ratio (SNR) considerations (18). This is especially true for preclinical studies where the typical ihMT signal in CNS tissues is half as low (10,18) as in humans (5,8). Thus, low RF duty-cycle approaches, which use bursts of very high peak-power RF pulses spaced widely over time are particularly appealing as they benefit from an enhanced sensitivity through the concentration of RF power during the off resonance saturation, thereby increasing the effects of dipolar order (12,14) and boosting the ihMT signal, in particular for the short T_{1D} components (17).

In this context, our study aimed at characterizing at constant high RF power and low duty-cycle saturation, the effect of T_{1D} filtering achieved with different values of Δt on ihMT signals from healthy myelinated CNS tissues, with the objective of identifying T_{1D}-

filters which can specifically isolate various ranges of T_{1D} components. Selection of filters and interpretation of results were guided by numerical simulations.

METHODS

Animal experiments

Animal studies were conducted on sixteen C57Bl/6J control mice (among them, 6 genetically modified mice expressed the green fluorescent protein (GFP) under the control of the *Plp* promoter which drives the expression of a major myelin component in the CNS – the proteolipid protein (PLP) (29)) and were performed in agreement with the French guidelines for animal care from the French Department of Agriculture (Animal Rights Division), the directive 2010/63/EU of the European Parliament and of the Council of 22 September 2010 and approved by our institutional committee on Ethics in animal research (Comité d'Ethique de Marseille n°14, project authorization APAFIS#1747-2015062215062372v6).

MRI protocol and analyses

Experimental setup

MR experiments were performed on a preclinical 7T scanner (PharmaScan, Bruker, Ettlingen, Germany). A 72 mm body volume coil (Bruker, Ettlingen, Germany) and a four-channel phased array receive-only MRI CryoProbe (Bruker, Ettlingen, Germany) were used for excitation and reception, respectively.

Mice were maintained under anesthesia during MR experiments by spontaneous respiration of a mixture of air and isoflurane (1.5%, constant flow, 300 mL/min; Univentor 400 anesthesia unit, Zejtun, Malta) through a dedicated nose cone. Ear bars were used to limit the mice head movement. Respiration and temperature were controlled throughout the experiments with an MR-compatible monitoring and gating system (SA Instruments, Stony Brook, NY, USA). A heating blanket connected to a water bath system was placed under the mice to carefully maintain a temperature of 37.5 ± 0.5 °C.

Experimental protocol

After positioning in the magnet isocenter, a field map-based shimming (acquisition time 1 min 22 s) was performed to optimize B_0 field homogeneity over the entire mouse brain. T_2-weighted (T_2w) structural images were acquired using a 2D multi-slice RARE sequence (RARE factor = 8, TE/TR = 32/5030 ms, matrix size 256x256, in-plane voxel size 78x78 μm^2, slice thickness 300 µm, 49 slices covering the whole brain, acquisition time TA = 5 mins 22 s). A B_1 map was acquired prior to the ihMT protocol using the Actual Flip Angle imaging method (30,31) ($TE/TR_1/TR_2$ = 2/15/60 ms, matrix size 48x48x44, 400x400x750 μm^3, FA = 60°, TA = 1 min 59 s). Slab-selective 3D low duty-cycle (12,14) ihMTRAGE sequences (22) (TE/TR = 2.1/2500.0 ms, matrix size 192x192x8, voxel size 100x100x750 μm^3) covering the whole corpus callosum were used to acquire ihMT images with four different configurations, corresponding to different Δt values.

The offset saturation pattern used in the ihMTRAGE sequences is provided in Figure 1. The single-offset saturation MT image (MT^{+}) was identical for all Δt values, whereas for dual-offset saturation MT images ($MT^{\pm}$), the application of cosine–modulated shaped pulses (CM), enabling saturation at both positive and negative frequency simultaneously, was used to virtually obtain a Δt of 0.0 ms (referenced hereafter by $\Delta t_{0.0}$). The use of alternated pulses with an increasing number of consecutive pulses of the same polarity (i.e., 1, 2 and 4) allowed to lengthen the value of Δt to 0.8 ms, 1.6 ms and 3.2 ms (referenced hereafter by $\Delta t_{0.8}$, $\Delta t_{1.6}$ and $\Delta t_{3.2}$, respectively).

Other saturation parameters were identical for all Δt values: Hann-shaped pulse duration (pw) of 0.5 ms (amplitude integral of 0.5 and power integral of 0.375 (5)); nominal peak pulse power (B_{1peak}) of 42.4 μT; root-mean-squared saturation power calculated over the total saturation time (B_{1RMS}^{SAT}) of 6.7 μT; frequency offset (Δf) of 10 kHz; number of pulses per burst (N_p) of 8; burst repetition time (BTR) of 60 ms; saturation time (τ) of 900 ms; number of bursts (N_{bursts}) of 15; and RF duty-cycle (DC) of 6.67%, calculated as:

$$DC = \frac{\Delta t * N_p * N_{bursts}}{\tau} \qquad \text{equation 1}$$

The acquisition time of each individual MT-weighted and MT_0 image was 20 s, hence leading to an acquisition time of 1 min 40 s for one ihMTR image. However, for SNR consideration, a total number of 6, 12, 12 and 18 repetitions of MT^{+}, MT^{-}, $MT^{\pm}$ and $MT^{\mp}$ images were acquired for the $\Delta t_{0.0}$, $\Delta t_{0.8}$, $\Delta t_{1.6}$ and $\Delta t_{3.2}$ ihMT images respectively,

leading to total acquisition times of 8 mins 40 s, 11 mins 20 s, 11 mins 20 s, and 22 mins.

Post-processing and statistical analysis

Template-based analyses were performed to quantitatively assess in different brain structures the ihMT ratio (ihMTR) values calculated for each of the four configurations:

$$ihMTR = \frac{(MT^{+} + MT^{-}) - (MT^{\pm} + MT^{\mp})}{MT_0} \qquad \text{equation 2}$$

where MT_0 is a reference image obtained without any saturation. A comprehensive description of the template construction and segmentation of the Regions-of-interest (ROIs) in seven different brain structures is provided in appendix A.

ROI-based statistical analyses were performed using the JMP software (15.1.0; SAS Institute, Cary, NC, USA). The mean values and group standard deviations were calculated for each brain structure and for each ihMT configuration.

For a straightforward analysis, ROIs were divided into three groups by their association to a specific tissue type: white matter, WM – containing myelinated structures and nerve fiber bundles (mCC – medial corpus callosum, INT – internal capsule and OPT – optical tract), grey matter, GM – containing structures mainly composed of neural and glial cells (CTX- cerebral cortex, HIP – hippocampal region), and mixed structures, Mix – containing structures with both WM and GM content (TH – thalamus, CP – caudoputamen).

Kolmogorov-Smirnov tests were performed for each ihMT modality to determine the normality of the distribution, and the homogeneity of variance was examined using the Bartlett test. The mean difference between the three groups of tissue types (WM, GM, and Mix) for each ihMT modality was tested first by a one-way Welch ANOVA test and was followed by post-hoc Games-Howell tests.

Simulations

The biophysical model associated with the theory of ihMT (2,32,33) for two non-null T_{1D} components (bi-T_{1D} model) is illustrated in Figure 2. According to the theory of weak RF saturation in solids advanced by Provotorov (34,35), the macromolecular pool of protons is divided into the semi-solid Zeeman and the dipolar order reservoirs, which are only coupled via RF induced transfer. The two dipolar compartments, β^{I1} and β^{I2} exchange with their associated semi-solid Zeeman compartment M_{ZB}^{I1} and M_{ZB}^{I2}, respectively. An additional semi-solid Zeeman reservoir (M_{ZB}^{H}) is assigned to account for macromolecular protons without any dipolar order contribution (e.g. $T_{1D} = 0$) (2). All macromolecular Zeeman orders exchange with the free liquid Zeeman compartment (M_{ZA}) through magnetization exchange. Modified Bloch-Provotorov equations in the matrix formalism (18,20,36) describe the evolution of the entire spin system:

$$\frac{dM_{ZA}}{dt} = R_{1A}(M_{0A} - M_{ZA}) - R(M_{0B}^{I1} + M_{0B}^{I2} + M_{0B}^{H})M_{ZA} + RM_{0A}(M_{ZB}^{I1} + M_{ZB}^{I2} + M_{ZB}^{H}) - R_{RFA}M_{ZA}$$

$$\frac{dM_{ZB}^{H}}{dt} = R_{1B}\left(M_{0B}^{H} - M_{ZB}^{H}\right) - RM_{0A}M_{ZB}^{H} + RM_{0B}^{H}M_{ZA} - R_{RFB}M_{ZB}^{H}$$

$$\frac{dM_{ZB}^{I1/I2}}{dt} = R_{1B}(M_{0B}^{I1/I2} - M_{ZB}^{I1/I2}) - RM_{0A}M_{ZB}^{I1/I2} + RM_{0B}^{I1/I2}M_{ZA} + 2\pi\Delta f R_{RFB}\beta^{I1/I2} - R_{RFB}M_{Z1B}^{I1/I2}$$

$$\frac{d\beta^{I1/I2}}{dt} = -\frac{1}{T_{1D}^{I1/I2}}\beta^{I1/I2} + R_{RFB}\frac{2\pi\Delta f}{D^2}M_{ZB}^{I1/I2} - R_{RFB}\left(\frac{2\pi\Delta f}{D}\right)^2\beta^{I1/I2}$$

Where M_{0A}, $M_{0B}^{H/I1/I2}$ represent the equilibrium magnetizations of each macromolecular compartment. M_{0B} represents the sum of individual M_{0B} values associated with each macromolecular compartment ($M_{0B} = M_{0B}^{H}+M_{0B}^{I1}+M_{0B}^{I2}$). Δf is the saturation frequency offset and D corresponds to the local dipolar field expressed in angular frequency units. To minimize the number of model parameters, all macromolecular reservoirs were assumed to be characterized by the same exchange and relaxation parameters. $R_{1A/B}$ is the relaxation rate of the liquid/macromolecular reservoir, R is the magnetization exchange rate between the liquid and macromolecular compartments and $R_{RFA/RFB}$ is the saturation rate of the liquid/macromolecular compartment, defined as:

$$R_{RFA/RFB} = \pi\omega_1^2 g_{A/B}(2\pi\Delta f),$$

where $g_{A/B}(2\pi\Delta f)$ is the liquid pool/semi-solid line shape and ω_1 the RF pulse intensity.

Previously, the matrix formalism enabled the calculation of an analytical steady state solution (18) allowing the calculation of the magnetization for each reservoir. Here, the same solution was implemented under Matlab (R2017b, MathWorks Inc., Natick, MA, USA) and the magnetization matrices dimensions were adjusted to include all the considered compartments.

The tissue parameters listed in Table 1 were fixed according to values reported in the literature for in vivo mouse brain imaging (2,10,37) and were also based on fitting on the $\Delta t_{3.2}$ configuration in WM and GM tissues. By convention, we chose $T_{1D}^{I1} < T_{1D}^{I2}$. T_{1D}^{I1} and T_{1D}^{I2} were considered as short T_{1D} if their value was smaller than 1 ms and long T_{1D} otherwise. For the simulated characterization, T_{1D}^{I1} or T_{1D}^{I2} were varied independently, while the other component was kept constant: when T_{1D}^{I1} was fixed to a short T_{1D} value (T_{1D}^{I1} < 1 ms), T_{1D}^{I2} was varied in the interval [T_{1D}^{I1}, 10 ms]; when T_{1D}^{I2} was fixed to a long T_{1D} value (T_{1D}^{I2} >1 ms), T_{1D}^{I1} was varied in the interval [0 µs, T_{1D}^{I2}]. For comparison with the experimental data, T_{1D}^{I1} and T_{1D}^{I2} were fixed to short T_{1D} and long T_{1D} values. In the absence of any quantification of the short T_{1D} component in the mouse brain, T_{1D}^{I1} was considered equal to values extracted from the rat spinal cord (T_{1D}^{I1} = 500 µs) (18). The long T_{1D} value was chosen based on previous T_{1D} measurements (T_{1D}^{I2} = 6 ms for WM) performed at 11.75T (10). Note that the field strength difference with the current study might result in a slight overestimation of T_{1D}, although the slow-motion processes occurring at the dipolar local field frequency, which do not scale with the B_0 intensity, are the main driving mechanism for T_{1D} relaxation (3,38). In addition, in reference (10), a single compartment model was used in combination with high RF power, that is conditions which slightly underestimate T_{1D} (18).

Simulations were performed for both WM and GM tissues, but due to the similarity in behavior henceforth results will mainly focus on WM. GM simulation curves are presented in Supporting Information Figure S1.

Finally, we arbitrarily defined a sensitivity threshold of 2% for ihMTR, corresponding to a value below which the ihMTR signal is considered as non-measurable.

RESULTS

Simulation results

General description of the T_{1D}-filtering strategy.

The lengthening of Δt created ihMT high-pass T_{1D}-filters characterized by T_{1D} cutoffs defined as values of T_{1D} for which ihMTR equals the 2%-threshold.

Let us first consider the case where one of the two compartments is associated with a null T_{1D} value (T_{1D}^{l1} = 0 ms). This simplified case allows us to study the effect of Δt on the long and short T_{1D} components separately. Incrementing Δt leads to an increase in the T_{1D} cutoff value, resulting in the removal of increasing ranges of T_{1D}s from the ihMT signal (Figure 3a). The cutoff values, indicated by colored dots on Figure 3a, achieved for the longer T_{1D}^{l2} component were shifted from 345 µs for $\Delta t_{0.0}$ to 620 µs for $\Delta t_{0.8}$ and to a maximum of 2.3 ms for $\Delta t_{3.2}$. Interestingly, if the ihMT high-pass T_{1D}-filters naturally eliminate the contribution from short T_{1D} components by attenuating their signal below the sensitivity threshold, they also attenuate the signal of longer T_{1D}s. Importantly, the attenuation of short and long T_{1D} components is however not uniform. This can be appreciated in Figure 3b, which shows ihMTR values normalized with respect to the $\Delta t_{0.0}$ configuration, the maximum ihMTR corresponding to each T_{1D} component at a given power. The decrease in ihMTR with increasing Δt is more important for short T_{1D}s (< 1 ms) compared to long T_{1D}s (≥ 1 ms). To give an order of

magnitude, quantitative values estimated for T_{1D}^{I2} = 500 µs and T_{1D}^{I2} = 6 ms are provided in Table 2.

Isolating long T_{1D} components and attenuating short T_{1D} components with ihMT high-pass T_{1D}-filters.

Let us now consider the case where T_{1D}^{I1} is no longer null but fixed to the in vivo short T_{1D} component value (T_{1D}^{I1} = 500 µs) and T_{1D}^{I2} variable (Figure 3c). The signal at the baseline (T_{1D}^{I1} = T_{1D}^{I2} = 500 µs) is higher, exceeding the 2%-threshold for all the Δt configurations except for $\Delta t_{3.2}$. The latter is the only configuration still allowing T_{1D}-filtering of short T_{1D}s with a cutoff value of T_{1D}^{I2} = 920 µs.

Figure 3d shows the ihMTR response to Δt for varying short T_{1D}^{I1} and fixed T_{1D}^{I2} (T_{1D}^{I2} = 6 ms). At T_{1D}^{I1} = 0 µs, the ihMTR values observed reflect the contribution of the fixed long 6 ms-T_{1D}^{I2} value only and, as T_{1D}^{I1} increased, the signal corresponding to this short T_{1D} component adds up to the baseline signal generated by the T_{1D}^{I2} component. The minimum value of T_{1D}^{I1} significantly contributing to the overall signal was determined for a total ihMTR value increased by 2% compared to the value at baseline (i.e., ihMTR value for T_{1D}^{I1} = 0 µs). It was shifted toward higher values as Δt increased (color points in Figure 3d), demonstrating once again, the filtering effect of Δt on the short T_{1D} components. The different contributions of short and long T_{1D} values in the total ihMTR signal depending on Δt can be inferred from Figure 3d and an example for in vivo conditions (T_{1D}^{I1} = 500 µs and T_{1D}^{I2} = 6 ms) is provided in Table 2.

Isolating short T_{1D} components with ihMT bandpass T_{1D}-filter.

Linear combinations between the signals achieved with $\Delta t_{0.0}$ and non-null Δt configurations enabled the generation of new filters. Remarkably, the ihMTR signal built upon the difference between the $\Delta t_{0.0}$ and $\Delta t_{0.8}$ resulted in an ihMT bandpass T_{1D}-filter which isolates short T_{1D} components, approximately within the 100 µs to 1 ms range (Figure 3e, green curve). Note that other Δt configurations used for differences with $\Delta t_{0.0}$ were unable to isolate narrow ranges of short T_{1D} values (Figure 3e, red and blue curves) as a result of diverging ihMTR values at extremity T_{1D}^{l1} values (Figure 3d).

Experimental results

Representative slices from the 3D templates of ihMT high-pass T_{1D}-filters clearly indicate a weaker signal and a varying contrast for increasing Δt values (Figure 4a). Additionally, Figure 4b presents ihMT bandpass T_{1D}-filters. Mean experimental ihMTR values in WM and GM computed from the average values measured in the seven segmented structures (summarized in Supporting Information Table S1) are plotted in Figure 5a and 5b for further comparison with simulation results (achieved for T_{1D}^{l1} = 500 µs and T_{1D}^{l2} = 6 ms).

The experimental WM/GM relative contrasts are presented in Figure 5c along with the simulated values. A very good agreement was obtained between experiments and simulations for both ihMTR and relative contrast values. Highest WM/GM relative contrast was obtained for the ihMT high-pass T_{1D}-filters in which the contribution of long T_{1D} components dominates the ihMT signal ($\Delta t \geq 1.6$ ms). On the other hand, the

lowest WM/GM relative contrast (< 0.2) was obtained for the ihMT bandpass T_{1D}-filter generated from the difference between $\Delta t_{0.0}$ and $\Delta t_{0.8}$ configurations, whose signal is dominated by T_{1D} components within the 100 µs to 1 ms range.

DISCUSSION

IhMT high-pass T_{1D}-filters with increasing cutoff values by means of Δt lengthening.

The use of frequency-alternated pulses to modulate the ihMT signal as a function of T_{1D} was first introduced as a strategy to quantify T_{1D} (8). Shortly after, the idea of using this sensitivity to filter out the ihMT signal and control the relative contrast of different tissues, based on the modification of the switching time Δt was proposed (10).

Here, the simulation results obtained with the bi-T_{1D} model including two non-null T_{1D} components provided a general understanding of the ihMTR signal response to the variation of the switching time (Figure 3). The lengthening of Δt allowed the generation of ihMT high-pass T_{1D}-filters with increasing cutoff values. This demonstrated the efficacy of Δt to eliminate the signal associated with T_{1D} values such that $T_{1D} << \Delta t$. In other words, Δt is the adjustment variable for the cutoff value of the ihMT high-pass T_{1D}-filter. However, this strategy also attenuates in some part the signal associated with longer T_{1D} values, as a consequence of an increasing dipolar order contribution in the dual-frequency MT images as Δt increased. This is clearly evidenced by the tendency of the dual-frequency MT signal shifting toward the single-frequency MT signal at longer Δt values (Supporting Information Figure S2).

Note that, in certain circumstances, a Δt of 0.0 ms as produced by CM pulses does not correspond to a T_{1D} cutoff of 0.0 ms (e.g., for T_{1D}^{l1} = 0 μs, the cutoff is obtained for T_{1D}^{l2} = 345 μs). This is a consequence of another filtering mechanism induced by the power effect that governs the existence of a dipolar order producing a measurable ihMT signal, by the empirical law $R_{RFB} \times T_{1D} > 0.01$ (28).

IhMT bandpass T_{1D}-filters for the isolation of short T_{1D} components can be generated with low duty-cycle and high-power approaches.

To isolate a range of short T_{1D} components through the simple subtraction between signals acquired with the $\Delta t_{0.0}$ and the non-null Δt configurations (Figure 3e), requires two main conditions to be met. First, a maximum signal for the short T_{1D} components in the $\Delta t_{0.0}$ configuration and second, a minimum attenuation of the long T_{1D} components for the ihMT high-pass T_{1D}-filters obtained with longer Δt values (Δt ≥ 0.8 ms) (Figure 3d). These two requisites are met for saturation schemes using high RF pulse power achieved in vivo with low RF duty-cycle conditions and non-null Δt values generating ihMT high-pass T_{1D}-filters with low cutoff values (Figure 3d).

Other circumstances, whether they concern different T_{1D} cutoffs or RF deposition schemes associated with lower RF pulse power are not appropriate. IhMT high-pass T_{1D}-filters with higher cutoff values (obtained with the $\Delta t_{1.6}$ and $\Delta t_{3.2}$ configurations, respectively) significantly attenuate the signal from long T_{1D} values (e.g., for T_{1D} = 6 ms, 25% attenuation for $\Delta t_{1.6}$ and 60% attenuation for $\Delta t_{3.2}$, in comparison to the $\Delta t_{0.8}$ configuration). This results in a gain of signal originating from the long T_{1D} components

in the subtraction filters rather than a bandpass shaped curve (Figure 3e). For an identical B_{1RMS}^{SAT} of 6.7 μT achieved with RF pulses fully distributed over the saturation period (DC = 62.5%) instead of concentrated RF pulses over the saturation period (DC = 6.67%), no isolation of components within the short T_{1D} range is possible (Figure 6b). At such a high DC value, the individual pulse power is reduced (13.8 μT for DC = 62.5% vs. 42.4 μT for DC = 6.67%) and fails to maximize the signal from short T_{1D} components in the $\Delta t_{0.0}$ configuration (Figure 6a, very close ihMTR values for all T_{1D}^{I1} values). Figures 6c, and 6d explore the possibility to isolate short T_{1D} components with B_{1RMS}^{SAT} values equivalent to those used in clinical studies (B_{1RMS}^{SAT} = 3 μT). Similar to what was observed for B_{1RMS}^{SAT} = 6.7 μT, a bandpass shape curve was obtained by a simple subtraction between $\Delta t_{0.0}$ and $\Delta t_{0.8}$ configurations, although the resulting ihMTR signal intensity was below the 2%-sensitivity threshold (Figure 6d). In this case again, the pulse power required to reach a B_{1RMS}^{SAT} = 3 μT was too low (19 μT) to maximize the signal from short T_{1D} components in the $\Delta t_{0.0}$ configuration (black curves, Figure 6c vs Figure 3d). However, we should recall that these simulations were obtained with MT parameters associated with mouse brain tissues, which differ from human values. In particular, the higher macromolecular fraction for the human brain WM (39) might generate higher ihMTR values, thereby allowing signal from subtraction filters above the sensitivity threshold even for the lower power acquisitions compatible with the clinical constraints. Thus, the viability of the ihMT bandpass T_{1D}-filters to isolate short T_{1D} components in humans warrants further dedicated studies.

The ihMT bandpass T_{1D}-filter based on the simple subtraction of $\Delta t_{0.0}$ and $\Delta t_{0.8}$ ihMTR images as proposed in this work required a rather long acquisition time (20 mins) and shows relatively modest SNR (maximum ihMTR values in the order of 7%). These performances could however be improved. From a technical perspective, the ihMT bandpass T_{1D}-filter does not require single frequency saturation images and could be built upon the difference of the dual offset saturation images only, thus gaining a factor of 2 in the acquisition time. Here, a basic linear combination was used to generate the ihMT bandpass T_{1D}-filter. However, the rather homogeneous behavior of ihMTR for all the values of Δt in the $T_{1D}^{l1} \geq 1$ ms range (Figure 3d) may suggest that combinations of several high-pass T_{1D}-filters with amplitudes multiplied by different factors could allow deriving more advanced filters. The purpose would be to provide a better cancellation of long T_{1D}s and consequently a better isolation of short T_{1D}s, preferably with a higher sensitivity. Nevertheless, such approaches rely on the amplitudes of the high-pass T_{1D}-filters, which are highly sensitive to the variations in some of the model parameters (Appendix B, Figure B1.a). Conversely, the shape of the proposed $\Delta t_{0.0} - \Delta t_{0.8}$ bandpass T_{1D}-filter to model parameters is less sensitive, as shown in Appendix B, Figure B1.d-e. This suggests the $\Delta t_{0.0} - \Delta t_{0.8}$ bandpass T_{1D}-filter as a more general and robust filter for the isolation of the short T_{1D} components.

T_{1D}-filtering at low duty-cycle offers more flexibility to modulate the relative WM/GM contrast by controlling the contributions of short and long T_{1D}s.

The bi-T_{1D} model allowed realistic simulations to be performed as indicated by the absolute signals and relative WM/GM contrast comparisons between the predicted and

experimental values (Figure 5). In terms of absolute ihMTR values, the best correspondence between simulations and experiments were obtained for the $\Delta t_{3.2}$ configuration for both WM and GM. Other configurations overestimated ($\Delta t_{0.8}$ and $\Delta t_{1.6}$) or underestimated ($\Delta t_{0.0}$) the experimental values. The tissue parameters used for the simulations were adapted from the literature and were also based on fitting on the $\Delta t_{3.2}$ configuration in WM and GM tissues, thus explaining the better match of this configuration between simulations and experiments. However, an incomplete model with insufficient T_{1D} compartments or even a higher sensitivity to some of the model parameters can have an impact on the comparison between experimental and simulated WM/GM contrasts. Although, it has been shown in ex-vivo studies of the spinal cord that ihMT approaches can be used to estimate two T_{1D} components with good sensitivity, in view of the NMR Jeener-Broekaert measurements which show a more continuous distribution of T_{1D}s (18), one cannot dismiss the fact that the ihMT signal might be influenced by other T_{1D} components as well. Furthermore, according to the sensitivity analysis (Appendix B, Figure B1), some of the model parameters have a significant influence on the absolute ihMTR signal. While it is true that most of the parameters with the highest sensitivity on the ihMT signal are also the ones that are best estimated with both qMT and qihMT models (such as T_{2B}), the existence of different species of macromolecules with various T_{2B} values has not been investigated thoroughly and might have an important influence on our results.

Previous in vivo studies on CNS tissues performed at high duty-cycle and high saturation power showed little difference in the relative WM/GM contrast when the

switching time was varied (10). In contrast, in the current study, the use of a low duty-cycle approach enabled a better differentiation between the signals of ihMT high-pass T_{1D}-filters, and thus a better differentiation between the resulted relative WM/GM contrasts. The ihMT high-pass T_{1D}-filters achieved with $\Delta t \geq 1.6$ ms presented the highest relative WM/GM contrast values, while for $\Delta t_{0.0}$ it was approximately 25% lower. Whereas similar results might be obtained at high duty-cycle by further increasing the pulse power, the advantage of low duty-cycle approaches is represented by the lower Specific Absorption Rates (SAR), particularly important for clinical translational studies and comparisons.

Limitations and future perspectives

Technical limitations related to the duration of the pulse and the inter-pulse delay (pw – Δt), constrain the minimum non-zero Δt value. Lower Δt values might enable the ihMT bandpass T_{1D}-filter to be shifted to ranges of shorter T_{1D} values. However, shorter pulses imply higher bandwidth, which depending on the frequency offset might lead to a direct saturation of the water protons. This effect is negligible for the current Hann-shaped pulses of 0.5 ms applied at ±10 kHz.

Quantification of the T_{1D} relaxation time characterizing different brain structures or any other model parameter is beyond the scope of this paper. Simulations were performed with MT parameters fixed to values reported in the literature to allow sensible association with the observed experimental behavior in CNS and assuming identical exchange and relaxation parameters for all macromolecular compartments. This last

hypothesis was meant to limit the number of model parameters. Since only four experimental points were acquired for comparisons with the simulated data, the sensitivity needed to distinguish between the different macromolecular species would be too low.

However, the effect of varying tissue model parameters on the amplitude and filter function of the various T_{1D}-filters proposed in this study were evaluated in a sensitivity analysis (Appendix B). Whereas the amplitudes of both the high-pass and bandpass T_{1D}-filters vary with the changes in model parameters, the filters' shape functions showed good robustness.

A detailed analysis on the explored filters' selectivity of certain T_{1D} components and their impact on the specificity and sensitivity of ihMT to myelin concerns the Part II of this work.

CONCLUSIONS

In conclusion, the present study characterized the ihMT high-pass T_{1D}-filtering effect induced by different switching time values and proposed an ihMT bandpass T_{1D}-filter based on the linear combination of signals acquired with different switching times. For the high instantaneous RF pulse powers achieved at low duty-cycle saturation, shorter T_{1D} components are substantial contributors to the signal of CNS tissue. IhMT high-pass T_{1D}-filters with high T_{1D} cutoff values can selectively image longer T_{1D} contributors and increase the WM/GM contrast, albeit at the cost of a loss in sensitivity. IhMT bandpass T_{1D}-filters can be used to isolate a range of shorter T_{1D} components that may

have other microstructural correlates than those of long T_{1D} components. Thus, T_{1D}-filtered ihMT imaging could be of particular interest in future studies on pathological models or in clinical applications, where the unstructured CNS tissues are expected to engender changes in the distribution of the T_{1D} components.

Appendix

Appendix A: Post-processing images

Schematics of the pipeline for template construction and atlas-based segmentation. Exported raw data was converted into the NIfTI format using the Dicomifier medical image converter (https://github.com/lamyj/dicomifier). After a quality check step, images were skull-stripped using an in-house script developed under Matlab (R2017b, MathWorks Inc., Natick, MA, USA). Individual 3D T_2w volumes were denoised with the BM4D algorithm (40) and corrected for the nonuniform signal intensity distribution using the N4ITK Bias Field Correction algorithm (41). Images were then registered onto an external template using ANTs (42) affine and non-linear iterative transformations. After cumulative averaging, a high resolution T_2w template representative of our mice population was obtained, which we called 16Bl6T_2w. Mouse-wise, all MT volumes were rigidly registered onto the MT_0 volume acquired immediately after the T_{2W} images, to minimize the distortions introduced by intra-scan movement in the estimated transformations. IhMTR maps were then calculated according to equation 1. The transformations estimated for the 16Bl6_T_2w template were afterwards applied on the calculated ihMTR volumes, and a first target ihMTR template was obtained in the same space as the 16Bl6_T_2w template. After

consecutive non-linear registrations and cumulative averaging, high resolution ihMTR templates were obtained for each ihMT modality, hereafter called 16Bl6_ihMTR template. Transformations were then estimated from the Dorr template to the 16Bl6_T_2w template and were then applied onto the Dorr labels to obtain a segmentation of the 16Bl6_T_2w template. The labels of interest were selected, manually corrected, and then propagated back into the space of each mouse for the quantification of ihMTR.

Appendix B: Robustness of T_{1D}-filters to tissue model parameters

Simulations were performed varying all model parameters by a factor of 0.5, 1.5 and 2 with respect to the fixed values reported in Table 1 in order to evaluate their respective influence on the shape and amplitude of the ihMT T_{1D}-filters. The T_{2B} and R values of the two macromolecular Zeeman compartments were also modified independently. The evolution of the $\Delta t_{3.2}$ high-pass and $\Delta t_{0.0} - \Delta t_{0.8}$ bandpass T_{1D}-filters with the variation of all model parameters are shown in the Supporting Information section (Supporting Information Figure S3 and Supporting Information Figure S4).

The changes in the shape of the filter function were analyzed by means of the so-called -3 dB point, which defines the filter cutoff corresponding to an attenuation of $\sqrt{2}$ of the maximum filter value. Therefore, we defined a filter cutoff for the high-pass T_{1D}-filter at -3 dB of the maximum of ihMTR at $T_{1D}{}^{I2}$ = 10 ms and a lower and upper filter cutoff for the band-pass T_{1D} filter at -3 dB from the maximum value of the filter determined for each investigated condition.

The absolute variations of the defined cutoffs are represented in Figure B1.b for the $\Delta t_{3.2}$ high-pass T_{1D}-filter and Figure B1.d, e for the bandpass T_{1D}-filter. The variation in the amplitude of the ihMTR signal corresponding to the two T_{1D}s equaling 6 ms and 500 µs (in vivo values) are represented in Figure B1.a for the $\Delta t_{3.2}$ high-pass T_{1D}-filter and in Figure B1.c for the bandpass T_{1D}-filter.

The amplitudes (ihMTR values) of both T_{1D}-filters varied with the model parameters. This is not surprising since several model parameters scale the ihMTR values. For instance, increasing the size of the macromolecular compartment associated with the long T_{1D} ($M_{0B}{}^{I2}$) naturally enhances the ihMTR values for the high-pass T_{1D} filter. However, and more importantly, the shape functions of the high-pass and bandpass T_{1D}-filters show a good robustness to the variations of model parameters. For the high-pass T_{1D}-filter, variations of the filter cutoff were less than 0.5 ms (Figure B1.b), and for the band-pass T_{1D}-filter, variations of the lower and upper filter cutoffs were less than 20 µs and 0.2 ms (Figure B1.d-e) respectively. The sensitivity to M_{0B}, T_{1D} and T_{2B} is more important, but the investigated range of variation [0.5 – 2] is not realistic in practice since it unlikely that M_{0B}, T_{1D} and T_{2B} are determined with such uncertainty (estimation errors are generally less than 10% as compared to the estimated value).

Acknowledgements

This work was funded by ANR-17-CE18-0030, VERISMO project and partly funded by France Life Imaging (grant ANR-11-INBS-0006), ARSEP 2021 and CARNOT STAR 2020. Authors thank Nathalie Cuge for animal handling.

References

1. Varma G, Duhamel G, de Bazelaire C, Alsop DC. Magnetization transfer from inhomogeneously broadened lines: A potential marker for myelin: Magnetization Transfer from Inhomogeneously Broadened Lines. Magn. Reson. Med. 2015;73:614–622 doi: 10.1002/mrm.25174.

2. Varma G, Girard OM, Prevost VH, Grant AK, Duhamel G, Alsop DC. Interpretation of magnetization transfer from inhomogeneously broadened lines (ihMT) in tissues as a dipolar order effect within motion restricted molecules. J. Magn. Reson. 2015;260:67–76 doi: 10.1016/j.jmr.2015.08.024.

3. Dufourc EJ, Mayer C, Stohrer J, Althoff G, Kothe G. Dynamics of phosphate head groups in biomembranes. Comprehensive analysis using phosphorus-31 nuclear magnetic resonance lineshape and relaxation time measurements. Biophys. J. 1992;61:42–57 doi: 10.1016/S0006-3495(92)81814-3.

4. Annabestani R, Cory D. Dipolar Relaxation Mechanism of Long Lived States in Methyl Groups. ArXiv170403035 Quant-Ph 2017.

5. Girard OM, Prevost VH, Varma G, Cozzone PJ, Alsop DC, Duhamel G. Magnetization transfer from inhomogeneously broadened lines (ihMT): Experimental optimization of saturation parameters for human brain imaging at 1.5 Tesla: Optimizing Saturation Parameters for ihMT Brain Imaging at 1.5T. Magn. Reson. Med. 2015;73:2111–2121 doi: 10.1002/mrm.25330.

6. Prevost VH, Girard OM, Varma G, Alsop DC, Duhamel G. Minimizing the effects of magnetization transfer asymmetry on inhomogeneous magnetization transfer (ihMT) at ultra-high magnetic field (11.75 T). Magn. Reson. Mater. Phys. Biol. Med. 2016;29:699–709 doi: 10.1007/s10334-015-0523-2.

7. Taso M, Girard OM, Duhamel G, et al. Tract-specific and age-related variations of the spinal cord microstructure: a multi-parametric MRI study using diffusion tensor imaging (DTI) and inhomogeneous magnetization transfer (ihMT): Spinal Cord Microstructure Assessment Using DTI and ihMT. NMR Biomed. 2016;29:817–832 doi: 10.1002/nbm.3530.

8. Varma G, Girard OM, Prevost VH, Grant AK, Duhamel G, Alsop DC. In vivo measurement of a new source of contrast, the dipolar relaxation time, T_{1D}, using a modified inhomogeneous magnetization transfer (ihMT) sequence: In Vivo Measurement of T_{1D} Using ihMT. Magn. Reson. Med. 2017;78:1362–1372 doi: 10.1002/mrm.26523.

9. Girard OM, Callot V, Prevost VH, et al. Magnetization transfer from inhomogeneously broadened lines (ihMT): Improved imaging strategy for spinal cord applications: ihMT for Spinal Cord Applications. Magn. Reson. Med. 2017;77:581–591 doi: 10.1002/mrm.26134.

10. Prevost VH, Girard OM, Mchinda S, Varma G, Alsop DC, Duhamel G. Optimization of inhomogeneous magnetization transfer (ihMT) MRI contrast for preclinical studies using dipolar relaxation time (T1D) filtering. NMR Biomed. 2017;30 doi: 10.1002/nbm.3706.

11. Rasoanandrianina H, Grapperon A-M, Taso M, et al. Region-specific impairment of the cervical spinal cord (SC) in amyotrophic lateral sclerosis: A preliminary study using SC

templates and quantitative MRI (diffusion tensor imaging/inhomogeneous magnetization transfer). NMR Biomed. 2017;30:e3801 doi: 10.1002/nbm.3801.

12. Mchinda S, Varma G, Prevost VH, et al. Whole brain inhomogeneous magnetization transfer (ihMT) imaging: Sensitivity enhancement within a steady-state gradient echo sequence: Whole Brain Inhomogeneous Magnetization Transfer (ihMT). Magn. Reson. Med. 2018;79:2607–2619 doi: 10.1002/mrm.26907.

13. Van Obberghen E, Mchinda S, le Troter A, et al. Evaluation of the Sensitivity of Inhomogeneous Magnetization Transfer (ihMT) MRI for Multiple Sclerosis. Am. J. Neuroradiol. 2018;39:634–641 doi: 10.3174/ajnr.A5563.

14. Varma G, Girard OM, Mchinda S, et al. Low duty-cycle pulsed irradiation reduces magnetization transfer and increases the inhomogeneous magnetization transfer effect. J. Magn. Reson. 2018;296:60–71 doi: 10.1016/j.jmr.2018.08.004.

15. Ercan E, Varma G, Mädler B, et al. Microstructural correlates of 3D steady-state inhomogeneous magnetization transfer (ihMT) in the human brain white matter assessed by myelin water imaging and diffusion tensor imaging: Ercan et al. Magn. Reson. Med. 2018;80:2402–2414 doi: 10.1002/mrm.27211.

16. Geeraert BL, Lebel RM, Mah AC, et al. A comparison of inhomogeneous magnetization transfer, myelin volume fraction, and diffusion tensor imaging measures in healthy children. NeuroImage 2018;182:343–350 doi: 10.1016/j.neuroimage.2017.09.019.

17. Duhamel G, Prevost VH, Cayre M, et al. Validating the sensitivity of inhomogeneous magnetization transfer (ihMT) MRI to myelin with fluorescence microscopy. NeuroImage 2019;199:289–303 doi: 10.1016/j.neuroimage.2019.05.061.

18. Carvalho VND, Hertanu A, Grélard A, et al. MRI assessment of multiple dipolar relaxation time (T 1 D) components in biological tissues interpreted with a generalized inhomogeneous magnetization transfer (ihMT) model. J. Magn. Reson. 2020;311:106668 doi: 10.1016/j.jmr.2019.106668.

19. Ercan E, Varma G, Dimitrov IE, et al. Combining inhomogeneous magnetization transfer and multipoint Dixon acquisition: Potential utility and evaluation. Magn. Reson. Med. 2020 doi: 10.1002/mrm.28571.

20. Malik SJ, Teixeira RPAG, West DJ, Wood TC, Hajnal JV. Steady-state imaging with inhomogeneous magnetization transfer contrast using multiband radiofrequency pulses. Magn. Reson. Med. 2020;83:935–949 doi: 10.1002/mrm.27984.

21. Wood TC, Damestani NL, Lawrence AJ, et al. Silent myelin-weighted magnetic resonance imaging. Wellcome Open Res. 2020;5:74 doi: 10.12688/wellcomeopenres.15845.1.

22. Varma G, Munsch F, Burns B, et al. Three-dimensional inhomogeneous magnetization transfer with rapid gradient-echo (3D ihMTRAGE) imaging. Magn. Reson. Med. 2020 doi: 10.1002/mrm.28324.

23. Munsch F, Varma G, Taso M, et al. Characterization of the cortical myeloarchitecture with inhomogeneous magnetization transfer imaging (ihMT). NeuroImage 2021;225:117442 doi: 10.1016/j.neuroimage.2020.117442.

24. Hou G, Lai W, Jiang W, et al. Myelin deficits in patients with recurrent major depressive disorder: An inhomogeneous magnetization transfer study. Neurosci. Lett. 2021;750:135768 doi: 10.1016/j.neulet.2021.135768.

25. Rowley CD, Campbell JSW, Wu Z, et al. A model-based framework for correcting inhomogeneity effects in magnetization transfer saturation and inhomogeneous magnetization transfer saturation maps. Magn. Reson. Med. n/a doi: https://doi.org/10.1002/mrm.28831.

26. Stadelmann C, Timmler S, Barrantes-Freer A, Simons M. Myelin in the Central Nervous System: Structure, Function, and Pathology. Physiol. Rev. 2019;99:1381–1431 doi: 10.1152/physrev.00031.2018.

27. de Campos Vidal B, Mello MLS, Caseiro-Filho AC, Godo C. Anisotropic properties of the myelin sheath. Acta Histochem. 1980;66:32–39 doi: 10.1016/S0065-1281(80)80079-1.

28. Manning AP, Chang KL, MacKay AL, Michal CA. The physical mechanism of "inhomogeneous" magnetization transfer MRI. J. Magn. Reson. 2017;274:125–136 doi: 10.1016/j.jmr.2016.11.013.

29. Greer JM, Lees MB. Myelin proteolipid protein—the first 50 years. Int. J. Biochem. Cell Biol. 2002;34:211–215 doi: 10.1016/S1357-2725(01)00136-4.

30. Yarnykh VL. Actual flip-angle imaging in the pulsed steady state: A method for rapid three-dimensional mapping of the transmitted radiofrequency field. Magn. Reson. Med. 2007;57:192–200 doi: 10.1002/mrm.21120.

31. Nehrke K. On the steady-state properties of actual flip angle imaging (AFI): Steady-State Properties of AFI. Magn. Reson. Med. 2009;61:84–92 doi: 10.1002/mrm.21592.

32. Yeung HN, Adler RS, Swanson SD. Transient Decay of Longitudinal Magnetization in Heterogeneous Spin Systems under Selective Saturation. IV. Reformulation of the Spin-Bath-Model Equations by the Redfield-Provotorov Theory. J. Magn. Reson. A 1994;106:37–45 doi: 10.1006/jmra.1994.1004.

33. Morrison C, Stanisz G, Henkelman RM. Modeling magnetization transfer for biological-like systems using a semi-solid pool with a super-Lorentzian lineshape and dipolar reservoir. J. Magn. Reson. B 1995;108:103–113 doi: 10.1006/jmrb.1995.1111.

34. Provotorov B. Magnetic resonance saturation in crystals. Zh Exsp Teor Fiz 1962;14:1126–1131.

35. Goldman M. Spin Temperature and Nuclear Magnetic Resonance in Solids. Oxford University Press.; 1970.

36. Portnoy S, Stanisz GJ. Modeling pulsed magnetization transfer. Magn. Reson. Med. 2007;58:144–155 doi: 10.1002/mrm.21244.

37. Soustelle L, Antal MC, Lamy J, Harsan L, Loureiro de Sousa P. Determination of optimal parameters for 3D single-point macromolecular proton fraction mapping at 7T in healthy and demyelinated mouse brain. Magn. Reson. Med. 2020 doi: 10.1002/mrm.28397.

38. Ueda T, Takeda S, Nakamura N, Chihara H. Molecular Motion and Phase Changes in Long Chain Solid Normal Alkanes as Studied by 1H and 13C NMR. Bull. Chem. Soc. Jpn. 1991;64:1299–1304 doi: 10.1246/bcsj.64.1299.

39. Yarnykh VL, Yuan C. Cross-relaxation imaging reveals detailed anatomy of white matter fiber tracts in the human brain. NeuroImage 2004;23:409–424 doi: 10.1016/j.neuroimage.2004.04.029.

40. Maggioni M, Katkovnik V, Egiazarian K, Foi A. A Nonlocal Transform-Domain Filter for Volumetric Data Denoising and Reconstruction. :15.

41. Tustison NJ, Avants BB, Cook PA, et al. N4ITK: Improved N3 Bias Correction. IEEE Trans. Med. Imaging 2010;29:1310–1320 doi: 10.1109/TMI.2010.2046908.

42. Avants BB, Tustison N, Song G. Advanced Normalization Tools (ANTS). :35.

Figure Captions

Main document

Figure 1: Schematics of a modified ihMT sequence used to derive ihMT images with different values of the frequency switching time Δt at constant RF power. (a) single-offset and (b-e) dual-offset preparations. RF saturation was achieved by means of bursts composed of 8 off-resonance pulses (N_p) with an offset frequency of 10 kHz (Δf) and a duration of 0.5 ms (pw), repeated every 60 ms (BTR), corresponding to an RF duty-cycle of 6.67% for a total saturation time of 900 ms (τ). Δt was lengthened from 0.8 ms to 1.6 ms and 3.2 ms by increasing the number of consecutive pulses of the same polarity from 1, 2 and 4. Cosine-modulated pulses producing simultaneous dual-offset saturation were used for Δt = 0.0 ms. For each Δt configuration, the ihMT image included the acquisition of two single frequency-offset (MT+ at +Δf and MT- at -Δf) and

two dual frequency-offset MT images to minimize the asymmetry of the macromolecular line (6).

Figure 2: Schematics of a bi-T_{1D} model (two non-null T_{1D} dipolar compartments) and the exchanges associated with the various compartments. Exchanges between the dipolar order compartments and their associated semi-solid Zeeman compartments are mediated by RF induced transfer. The liquid compartment exchanges with Zeeman compartments through magnetization transfer. Zeeman semi-solid reservoirs were assumed to be characterized by the same relaxation parameters, saturation rate and exchange rate with the Zeeman liquid reservoir.

Figure 3: Simulated behavior of ihMTR for four values of Δt (0.0 ms, 0.8 ms, 1.6 ms and 3.2 ms) at low RF duty cycle (6.67%) and high power (6.7 μT). (a) T_{1D}^{l1} is fixed at 0 ms, and T_{1D}^{l2} is varied in a range of short and long T_{1D} values. The colored dots indicate the shift in T_{1D} cutoff corresponding to the 2%-ihMTR detectability threshold. (b) The curves from point (a) normalized with respect to the $\Delta t_{0.0}$ configuration illustrate the higher signal attenuation of the short T_{1D}s as compared to the long components for increasing Δts. (c) T_{1D}^{l1} is fixed at 500 μs and the longer T_{1D}^{l2} component is varied in the [T_{1D}^{l1}, 10 ms] range. The red dot corresponds to the 2%-ihMTR detectability threshold for the high-pass $\Delta t_{3.2}$ T_{1D}-filter. (d) T_{1D}^{l2} is fixed to the long value of 6.0 ms and the shorter T_{1D}^{l1} component is varied in the [0.0 μs, T_{1D}^{l2}] range *(*data not shown on the graph – T_{1D}^{l1} starts from 10 μs for the sake of viewing*)*. Colored dots indicate an increase of 2% (in absolute ihMTR unit) as compared to the baseline. (e) Band-

pass T_{1D} filters calculated from subtraction between ihMTR obtained with $\Delta t = 0.0$ ms and ihMTR obtained with $\Delta t \geq 0.8$ ms for the same range of T_{1D}^{I1} values.

Figure 4: Experimental ihMTR maps illustrate the signal intensity and contrast achieved on the brain of control mice with (a) increasing switching time values (b) the difference between the $\Delta t = 0.0$ ms and $\Delta t \geq 0.8$ ms configurations. Slices are presented from the anterior (+0.25 mm from bregma) to the posterior (-3.20 mm from bregma) part of the brain and the acquisition time is indicated for each ihMT configuration.

Figure 5: Absolute ihMTR values obtained in (a) GM and (b) WM experimentally (blue) and simulated (orange) with the bi-T_{1D} model for all ihMT configurations. (c) Experimental (blue) and simulated (orange) relative WM/GM contrast calculated as (ihMTRWM - ihMTRGM)/ihMTRWM. The errors on the experimental signals represent the standard deviations on the entire population of 16 mice, while for the simulated signals the standard deviations were calculated on multiple simulations with T_{1D} values varying in the range of the estimated fit errors (± 1 ms for the long T_{1D}^{I2} component and ± 100 µs for the short T_{1D}^{I1} component) (10,19).

Figure 6: IhMTR as a function of T_{1D}^{I1} simulated with the bi-T_{1D} model and T_{1D}^{I2} fixed at 6.0 ms for the four Δt configurations and ihMTR calculated from subtraction between $\Delta t = 0.0$ ms and $\Delta t > 0$ ms configurations at: (a, b) High power (6.7 µT) and high DC (62.5%) and (c, d) Low power (3 µT) and low DC (6.67%).

Table 1: Model parameters used for the simulation of WM and GM tissues with the the bi-T_{1D} model. The non-null M_{0B} is distributed between all the macromolecular compartments ($M_{0B} = M_{0B}^{H} + M_{0B}^{I1} + M_{0B}^{I2}$). The two T_{1D} components are either varied in indicated ranges, either fixed for comparison with experimental data.

Table 2: Differential effect of Δt on short and long T_{1D} components. On the left side, quantifications of ihMTR at various Δts for a T_{1D}^{I1} component of 0 µs and two T_{1D}^{I2} components of 6 ms (long T_{1D}) and 500 µs (short T_{1D}), extracted from Figure 3a. The normalized (Norm. ihMTR) and attenuated signals (Signal loss) were calculated with respect to the $\Delta t_{0.0}$ configuration. On the right side, for each Δt value, the contribution of short and long T_{1D}s to the total ihMTR signal corresponding to in vivo conditions (T_{1D}^{I1} = 500 µs; T_{1D}^{I2} = 6 ms), extracted from Figure 3d. The contribution of the long T_{1D} component to the ihMTR signal was calculated as the ratio between the ihMTR values obtained for (T_{1D}^{I1} = 0 µs and T_{1D}^{I2} = 6 ms) and the ihMTR values obtained for (T_{1D}^{I1} = 500 µs and T_{1D}^{I2} = 6 ms).

Appendix

Figure A1: Pipeline for template construction and segmentation. Native T_2w and MT volumes were processed with the purpose of obtaining T_2w and ihMTR templates in the same space (16Bl6_T2w and 16Bl6_ihMTR). The Dorr atlas was used afterwards to obtain segmentations of the structures of interest.

Figure B1: Variation of the absolute ihMTR signal amplitudes of the (a) $\Delta t_{3.2}$ high-pass and (c) the $\Delta t_{0.0}$ – $\Delta t_{0.8}$ bandpass T_{1D}-filters for the in vivo conditions and all model

parameters. Analysis of the filter function for (b) the $\Delta t_{3.2}$ high-pass and (d, e) the $\Delta t_{0.0}$ – $\Delta t_{0.8}$ band-pass T_{1D}-filters for all model parameters. Dark points are associated with the fixed model parameters and the colored points illustrate the fixed parameter multiplied by a factor of 0.5 (blue), 1.5 (green) and 2 (orange).

Supporting Information

Table S1: Quantitative ihMTR metrics (mean ± standard deviation) in the selected brain anatomical structures of healthy mice (n = 16) and for each group of tissue type, where INT – internal capsule, mCC – medial corpus callosum, OPT – optical tract, TH – thalamus, CP – caudoputamen, CTX – cerebral cortex, HIP – hippocampal region, WM = mean [internal capsule, corpus callosum, optical tract], GM = mean [cerebral cortex, hippocampal region] and Mix = mean [thalamus, caudoputamen]. Significant differences between the mean values of each group of tissue are indicated as: § - significant difference to WM, * - significant difference to Mix, # - significant difference to GM.

Figure S1: Bi-T_{1D} model simulation for GM tissue parameters. (a) Simulated behavior of ihMTR for four values of Δt (0.0 ms, 0.8 ms, 1.6 ms and 3.2 ms) at low RF duty cycle (6.67%) and high power (6.7 μT) when T_{1D}^{I2} is fixed to the long value of 5.8 ms and the shorter T_{1D}^{I1} component is varied in the [10.0 μs, 1.0 ms] range (b) ihMTR calculated from subtraction between ihMTR obtained with Δt = 0.0 ms and ihMTR obtained with Δt > 0 ms for the same range of T_{1D}^{I1} values.

Figure S2: The evolution of MT^{+} and $MT^{\pm}$ as a function of T_{1D}^{I1} for the bi-T_{1D} model and WM tissue parameters. Increasing Δt leads to a less efficient $MT^{\pm}$ saturation, which approached the MT^{+} curve, resulting besides the natural filtering of short T_{1D} components into a supplementary filtering of long T_{1D} components. T_{1D}^{I2} is fixed at 6 ms, while T_{1D}^{I1} is varied in the [10 µs; 1ms] range.

Figure S3: The variation of the high-pass $\Delta t_{3.2}$ T_{1D}-filter shape with varying model parameters.

Figure S4: The variation of the band-pass $\Delta t_{0.0}$ – $\Delta t_{0.8}$ T_{1D}-filter shape with varying model parameters.

Table 1: Model parameters used for the simulation of WM and GM tissues with the the bi-T_{1D} model. The non-null M_{0B} is distributed between all the macromolecular compartments ($M_{0B} = M_{0B}^{H} + M_{0B}^{I1} + M_{0B}^{I2}$). The two T_{1D} components are either varied in indicated ranges, either fixed for comparison with experimental data.

											Variation in a large range		Comparison with experiments	
	T_{1A} (s)	T_{2A} (ms)	T_{1B} (s)	T_{2B} (µs)	R (s^{-1})	M_{0A}	M_{0B}	M_{0B}^{I1}	M_{0B}^{I2}	M_{0B}^{H}	T_{1D}^{I1}	T_{1D}^{I2}	T_{1D}^{I1} (µs)	T_{1D}^{I2} (ms)
WM	1.7	22.1	1	9	60	1	0.100	0.075	0.025	0.000	[0 µs;	[T_{1D}^{I1};	500	6
GM	2	30		8	50		0.035	0.028	0.005	0.003	T_{1D}^{I2}]	10 ms]	400	5.8

Table 2: Differential effect of Δt on short and long T_{1D} components. On the left side, quantifications of ihMTR at various Δts for a T_{1D}^{I1} component of 0 μs and two T_{1D}^{I2} components of 6 ms (long T_{1D}) and 500 μs (short T_{1D}), extracted from Figure 3a. The normalized (Norm. ihMTR) and attenuated signals (Signal loss) were calculated with respect to the $\Delta t_{0.0}$ configuration. On the right side, for each Δt value, the contribution of short and long T_{1D}s to the total ihMTR signal corresponding to in vivo conditions (T_{1D}^{I1} = 500 μs; T_{1D}^{I2} = 6 ms), extracted from Figure 3d. The contribution of the long T_{1D} component to the ihMTR signal was calculated as the ratio between the ihMTR values obtained for (T_{1D}^{I1} = 0 μs and T_{1D}^{I2} = 6 ms) and the ihMTR values obtained for (T_{1D}^{I1} = 500 μs and T_{1D}^{I2} = 6 ms).

	ihMTR signal attenuation for long and short T_{1D} components				Contribution of long and short T_{1D} components to the ihMTR signal			
	T_{1D}^{I1} = 0 μs; T_{1D}^{I2} = 6 ms		T_{1D}^{I1} = 0 μs; T_{1D}^{I2} = 500 μs		ihMTR (%) T_{1D}^{I1} = 0 μs, T_{1D}^{I2} = 6 ms	ihMTR (%) T_{1D}^{I1} = 500 μs, T_{1D}^{I2} = 6 ms	% contribution of long T_{1D}	% contribution of short T_{1D}
	Norm. ihMTR (%)	Signal loss w/r $\Delta t_{0.0}$ (%)	Norm. ihMTR (%)	Signal loss w/r $\Delta t_{0.0}$ (%)				
$\Delta t_{0.0}$	100	0	100	0	8.0	19.0	42	58
$\Delta t_{0.8}$	93.15	6.85	57.16	42.84	7.5	14.9	50	50
$\Delta t_{1.6}$	77.46	22.54	30.78	69.22	6.2	11.1	56	44
$\Delta t_{3.2}$	41.12	58.88	10.75	89.25	3.3	5.3	62	38

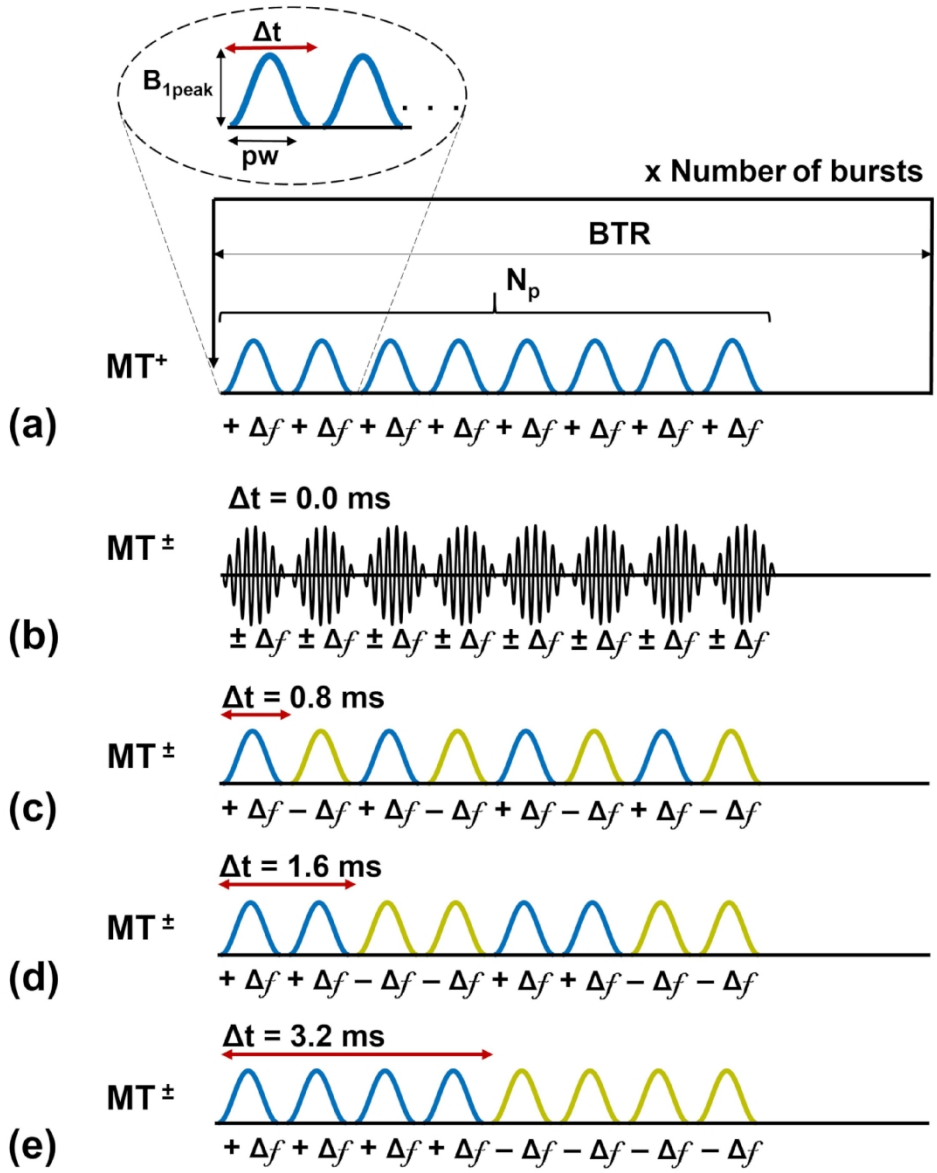

Figure 1: Schematics of a modified ihMT sequence used to derive ihMT images with different values of the frequency switching time Δt at constant RF power. (a) Single-offset and (b-e) dual-offset preparations. RF saturation was achieved by means of bursts composed of 8 off-resonance pulses (N_p) with an offset frequency of 10 kHz (Δf) and a duration of 0.5 ms (pw), repeated every 60 ms (BTR), corresponding to an RF duty-cycle of 6.67% for a total saturation time of 900 ms (τ). Δt was lengthened from 0.8 ms to 1.6 ms and 3.2 ms by increasing the number of consecutive pulses of the same polarity from 1, to 2 and 4. Cosine-modulated pulses producing simultaneous dual-offset saturation were used for Δt = 0.0 ms. For each Δt configuration, the ihMT image included the acquisition of two single frequency-offset (MT^+ at +Δf and MT^- at -Δf) and two dual frequency-offset MT images to minimize the asymmetry of the macromolecular line (6).

130x161mm (600 x 600 DPI)

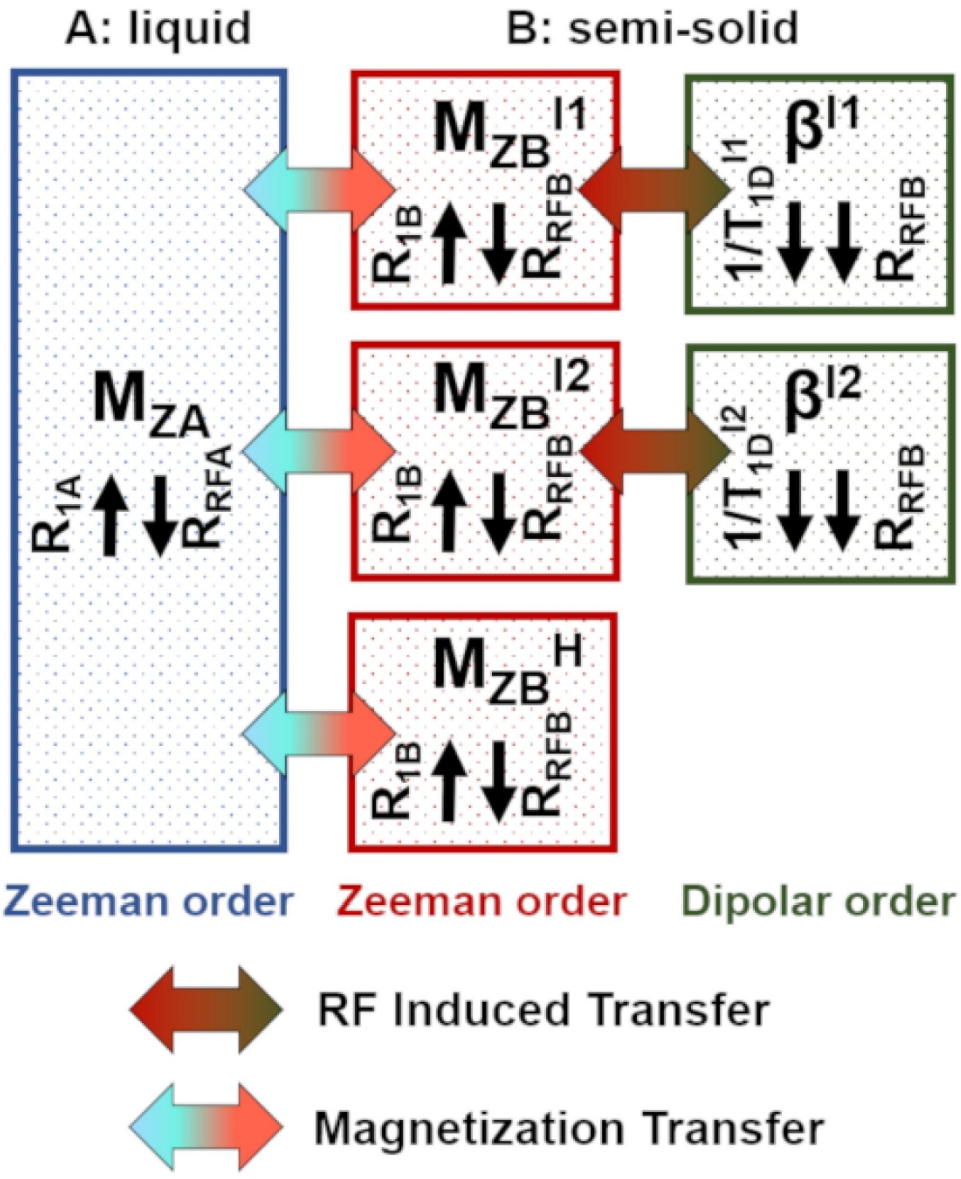

Figure 2: Schematics of a bi-T_{1D} model (two non-null T_{1D} dipolar compartments) and the exchanges associated with the various compartments. Exchanges between the dipolar order compartments and their associated semi-solid Zeeman compartments are mediated by RF induced transfer. The liquid compartment exchanges with Zeeman compartments through magnetization transfer. Zeeman semi-solid reservoirs were assumed to be characterized by the same relaxation parameters, saturation rate and exchange rate with the Zeeman liquid reservoir.

86x105mm (600 x 600 DPI)

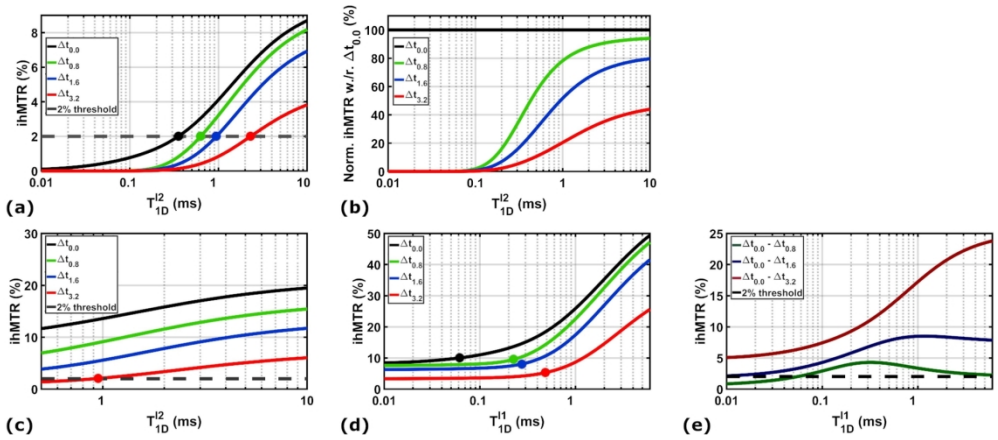

Figure 3: Simulated behavior of ihMTR for four values of Δt (0.0 ms, 0.8 ms, 1.6 ms and 3.2 ms) at low RF duty cycle (6.67%) and high power (6.7 μT). (a) T_{1D}^{I1} is fixed at 0 ms, and T_{1D}^{I2} is varied in a range of short and long T_{1D} values. The colored dots indicate the shift in T_{1D} cutoff corresponding to the 2%-ihMTR detectability threshold. (b) The curves from point (a) normalized with respect to the $\Delta t_{0.0}$ configuration illustrate the higher signal attenuation of the short T_{1D}s as compared to the long components for increasing Δts. (c) T_{1D}^{I1} is fixed at 500 μs and the longer T_{1D}^{I2} component is varied in the [T_{1D}^{I1}, 10 ms] range. The red dot corresponds to the 2%-ihMTR detectability threshold for the high-pass $\Delta t_{3.2}$ T_{1D}-filter. (d) T_{1D}^{I2} is fixed to the long value of 6.0 ms and the shorter T_{1D}^{I1} component is varied in the [0.0 μs, T_{1D}^{I2}] range (data not shown on the graph – T_{1D}^{I1} starts from 10 μs for the sake of viewing). Colored dots indicate an increase of 2% (in absolute ihMTR unit) as compared to the baseline. (e) Band-pass T_{1D} filters calculated from subtraction between ihMTR obtained with Δt = 0.0 ms and ihMTR obtained with Δt ≥ 0.8 ms for the same range of T_{1D}^{I1} values.

172x75mm (300 x 300 DPI)

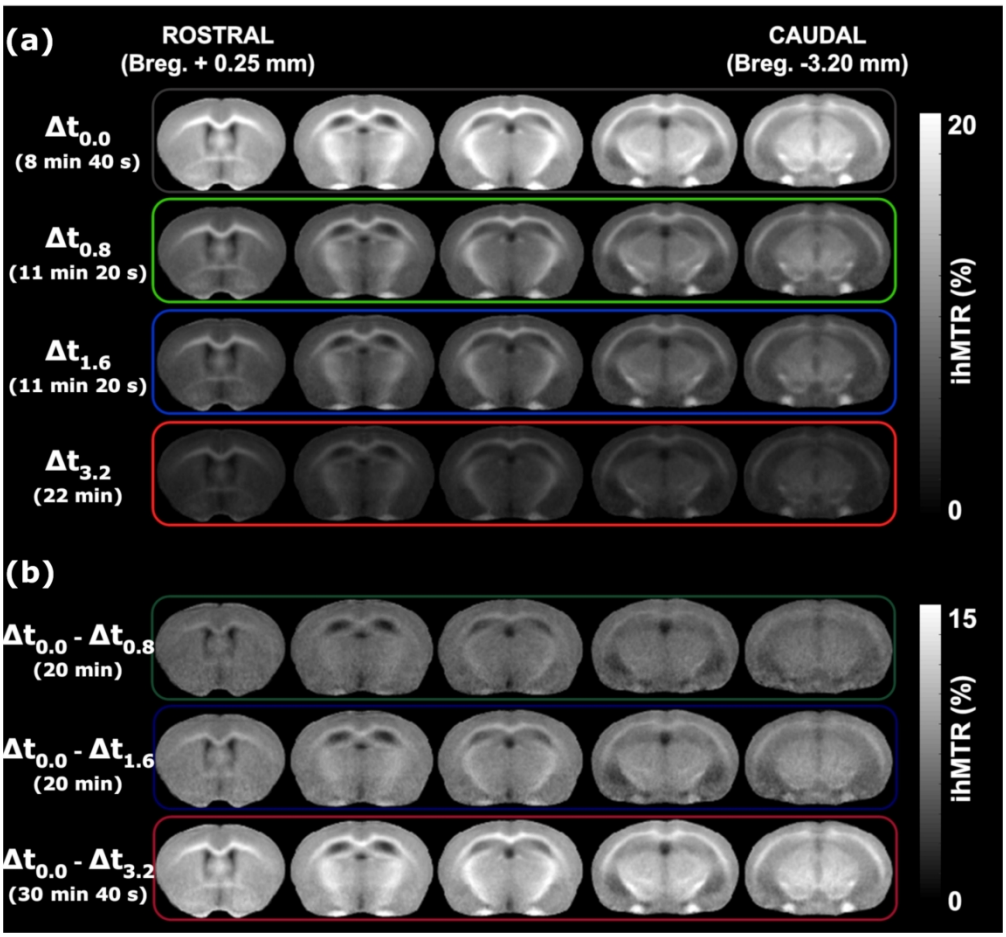

Figure 4: Experimental ihMTR maps illustrate the signal intensity and contrast achieved on the brain of control mice with (a) increasing switching time values (b) the difference between the Δt = 0.0 ms and Δt ≥ 0.8 ms configurations. Slices are presented from the anterior (+0.25 mm from bregma) to the posterior (-3.20 mm from bregma) part of the brain and the acquisition time is indicated for each ihMT configuration.

175x162mm (300 x 300 DPI)

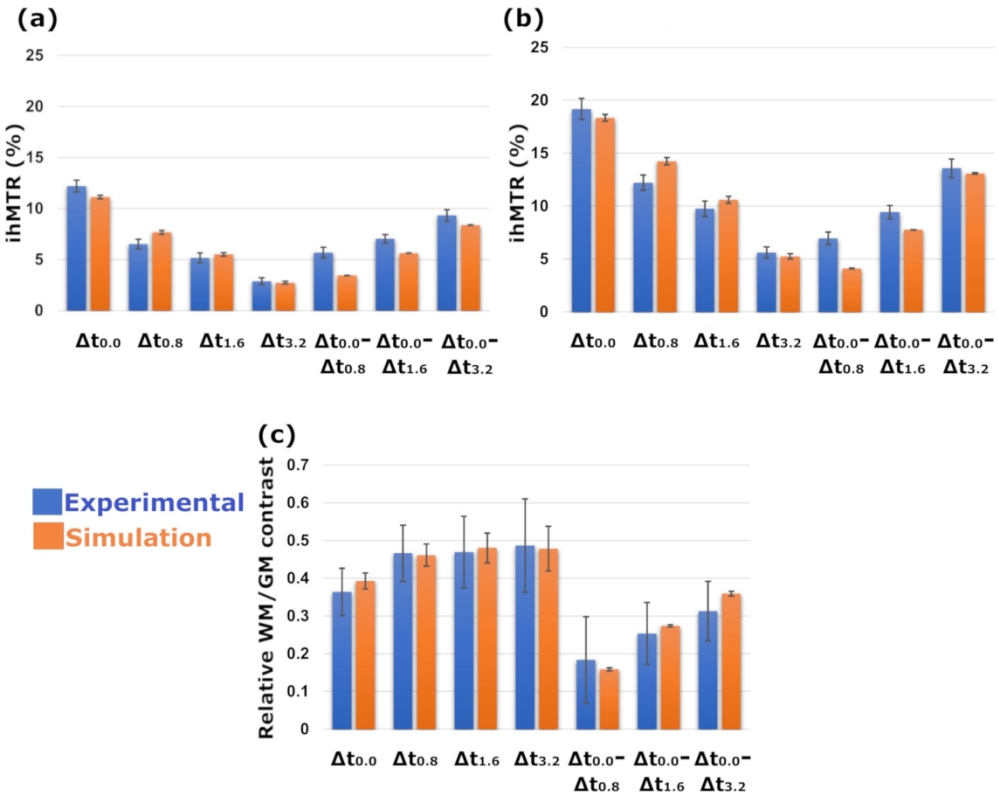

Figure 5: Absolute ihMTR values obtained in (a) GM and (b) WM experimentally (blue) and simulated (orange) with the bi-T_{1D} model for all ihMT configurations. (c) Experimental (blue) and simulated (orange) relative WM/GM contrast calculated as ($ihMTR_{WM}$ - $ihMTR_{GM}$)/$ihMTR_{WM}$. The errors on the experimental signals represent the standard deviations on the entire population of 16 mice, while for the simulated signals the standard deviations were calculated on multiple simulations with T_{1D} values varying in the range of the estimated fit errors (± 1 ms for the long T_{1D}^{I2} component and ± 100 µs for the short T_{1D}^{I1} component) (10,19).

175x141mm (300 x 300 DPI)

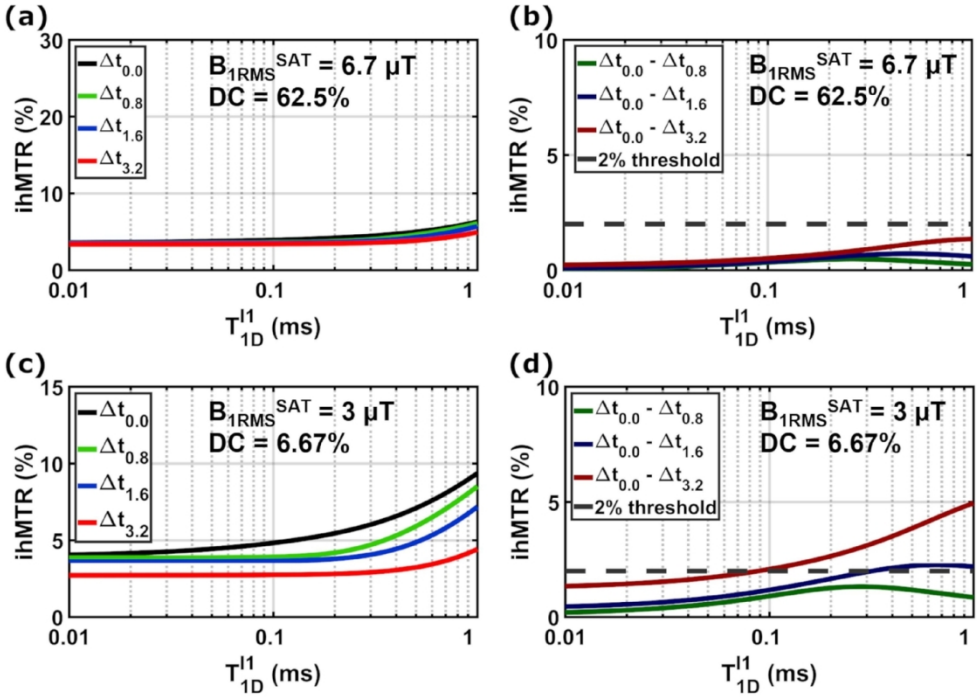

Figure 6: IhMTR as a function of T_{1D}^{I1} simulated with the bi-T_{1D} model and T_{1D}^{I2} fixed at 6.0 ms for the four Δt configurations and ihMTR calculated from subtraction between Δt = 0.0 ms and Δt > 0 ms configurations at: (a, b) High power (6.7 μT) and high DC (62.5%) and (c, d) Low power (3 μT) and low DC (6.67%).

130x93mm (300 x 300 DPI)

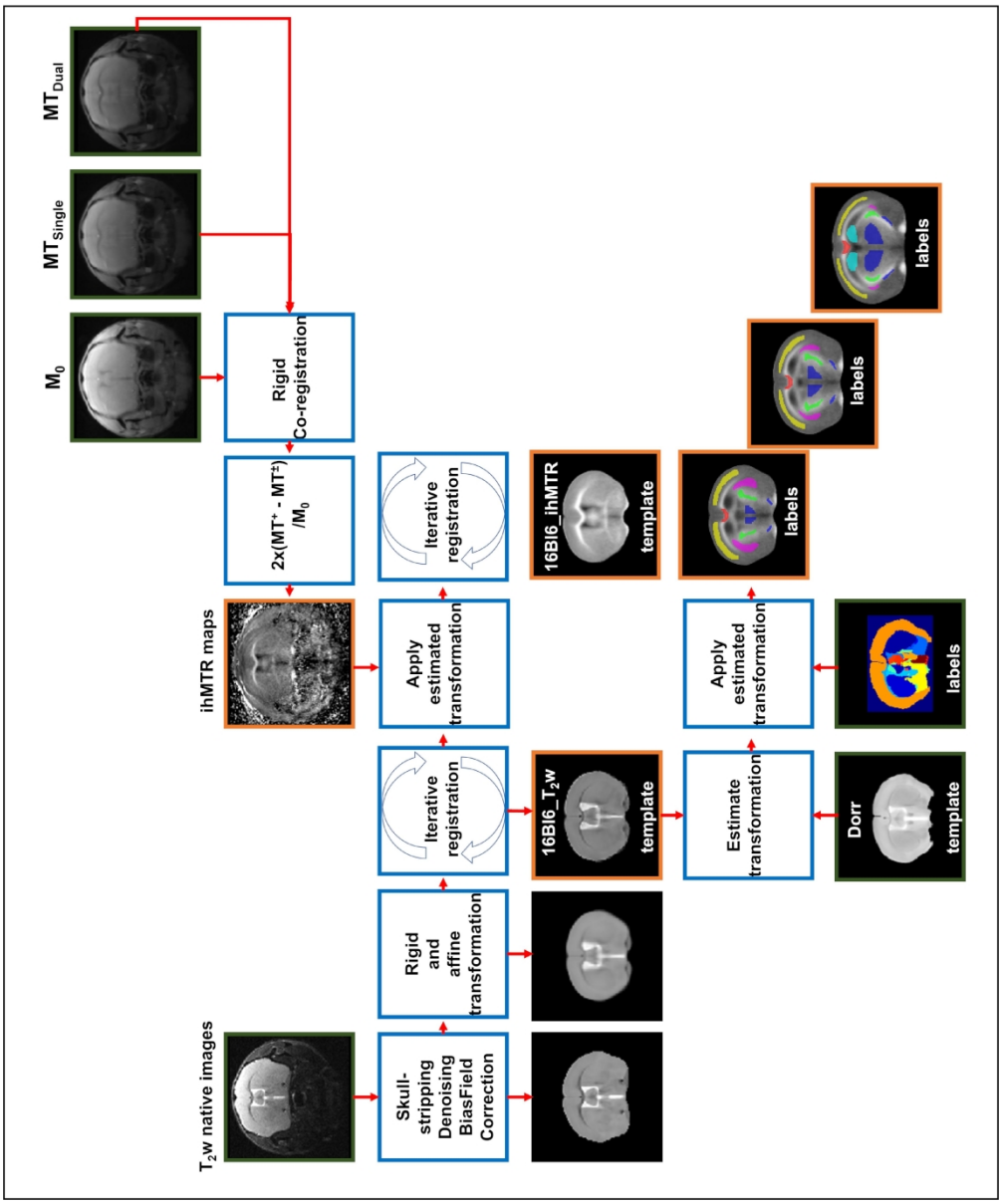

Figure A1: Pipeline for template construction and segmentation. Native T_2w and MT volumes were processed with the purpose of obtaining T_2w and ihMTR templates in the same space (16Bl6_T_2w and 16Bl6_ihMTR). The Dorr atlas was used afterwards to obtain segmentations of the structures of interest.

175x210mm (600 x 600 DPI)

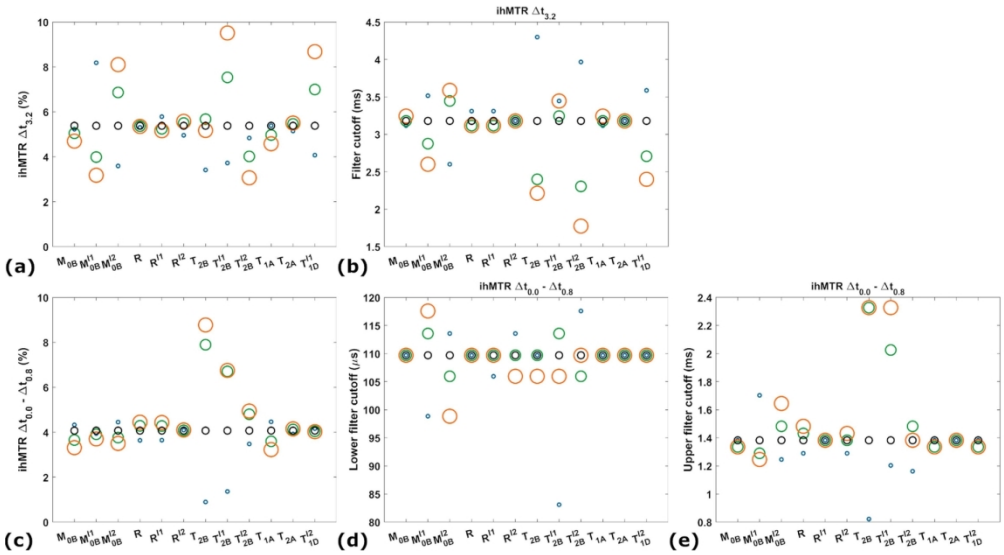

Figure B1: Variation of the absolute ihMTR signal amplitudes of the (a) $\Delta t_{3.2}$ high-pass and (c) the $\Delta t_{0.0} - \Delta t_{0.8}$ bandpass T_{1D}-filters for the in vivo conditions and all model parameters. Analysis of the filter function for (b) the $\Delta t_{3.2}$ high-pass and (d, e) the $\Delta t_{0.0} - \Delta t_{0.8}$ band-pass T_{1D}-filters for all model parameters. Dark points are associated with the fixed model parameters and the colored points illustrate the fixed parameter multiplied by a factor of 0.5 (blue), 1.5 (green) and 2 (orange).

161x89mm (300 x 300 DPI)

Supporting Information

A summary of the mean ihMTR values and standard deviations in each of the seven segmented structures is presented in Table S1. Quantifications were performed on each mouse brain. WM tissues present higher ihMTR values than Mix tissues, which in turn present higher values than GM tissues for all Δt values. Standard deviations are lower than 1% and generally do not exceed 15% of the mean ihMTR value. All data was found to be normally distributed ($p > 0.05$) and heteroscedastic ($p > 0.05$). The analysis of variance and the post-hoc tests revealed significant differences ($p < 0.001$) between the three groups for all Δt configurations.

Table S1: Quantitative ihMTR metrics (mean ± standard deviation) in the selected brain anatomical structures of healthy mice (n = 16) and for each group of tissue type, where INT – internal capsule, mCC – medial corpus callosum, OPT – optical tract, TH – thalamus, CP – caudoputamen, CTX – cerebral cortex, HIP – hippocampal region, WM = mean [internal capsule, corpus callosum, optical tract], GM = mean [cerebral cortex, hippocampal region] and Mix = mean [thalamus, caudoputamen]. Significant differences between the mean values of each group of tissue are indicated as: § - significant difference to WM, * - significant difference to Mix, # - significant difference to GM.

	INT	mCC	OPT	WM	TH	CP	Mix	CTX	HIP	GM
$\Delta t_{0.0}$	19.78 ± 0.70	19.24 ± 0.97	18.50 ± 0.87	19.17 ± 0.99 *#	14.05 ± 0.44	13.12 ± 0.38	13.58 ± 0.62 §#	12.21 ± 0.52	12.20 ± 0.65	12.20 ± 0.58 §*
$\Delta t_{0.8}$	12.64 ± 0.40	12.35 ± 0.74	11.64 ± 0.55	12.21 ± 0.71 *#	7.91 ± 0.39	7.27 ± 0.27	7.59 ± 0.46 §#	6.58 ± 0.52	6.46 ± 0.42	6.52 ± 0.47 §*

$\Delta t_{1.6}$	10.03 ± 0.61	10.06 ± 0.51	9.14 ± 0.64	9.74 ± 0.72 *#	6.23 ± 0.53	5.73 ± 0.24	5.99 ± 0.48 §#	5.18 ± 0.51	5.15 ± 0.43	5.17 ± 0.47 §*
$\Delta t_{3.2}$	5.76 ± 0.43	5.83 ± 0.32	5.25 ± 0.65	5.61 ± 0.54 *#	3.59 ± 0.35	3.16 ± 0.27	3.38 ± 0.37 §#	2.96 ± 0.33	2.81 ± 0.37	2.88 ± 0.35 §*
$\Delta t_{0.0} - \Delta t_{3.2}$	14.02 ± 0.67	13.40 ± 1.03	13.26 ± 0.70	13.56 ± 0.87 *#	10.46 ± 0.49	9.96 ± 0.29	10.21 ± 0.47 §#	9.25 ± 0.43	9.39 ± 0.66	9.32 ± 0.56 §*
$\Delta t_{0.0} - \Delta t_{1.6}$	9.75 ± 0.38	9.18 ± 0.75	9.36 ± 0.60	9.43 ± 0.63 *#	7.82 ± 0.42	7.38 ± 0.43	7.60 ± 0.47 §#	7.03 ± 0.31	7.05 ± 0.52	7.04 ± 0.42 §*
$\Delta t_{0.0} - \Delta t_{0.8}$	7.14 ± 0.66	6.88 ± 0.58	6.86 ± 0.53	6.96 ± 0.59 *#	6.14 ± 0.33	5.85 ± 0.34	6.00 ± 0.36 §#	5.63 ± 0.51	5.74 ± 0.54	5.68 ± 0.52 §*

Figure S1: Bi-T_{1D} model simulation for GM tissue parameters. (a) Simulated behavior of ihMTR for four values of Δt (0.0 ms, 0.8 ms, 1.6 ms and 3.2 ms) at low RF duty cycle (6.67%) and high power (6.7 μT) when T_{1D}^{I2} is fixed to the long value of 5.8 ms and the shorter T_{1D}^{I1} component is varied in the [10.0 μs, 1.0 ms] range (b) ihMTR calculated from subtraction between ihMTR obtained with Δt = 0.0 ms and ihMTR obtained with Δt > 0 ms for the same range of T_{1D}^{I1} values.

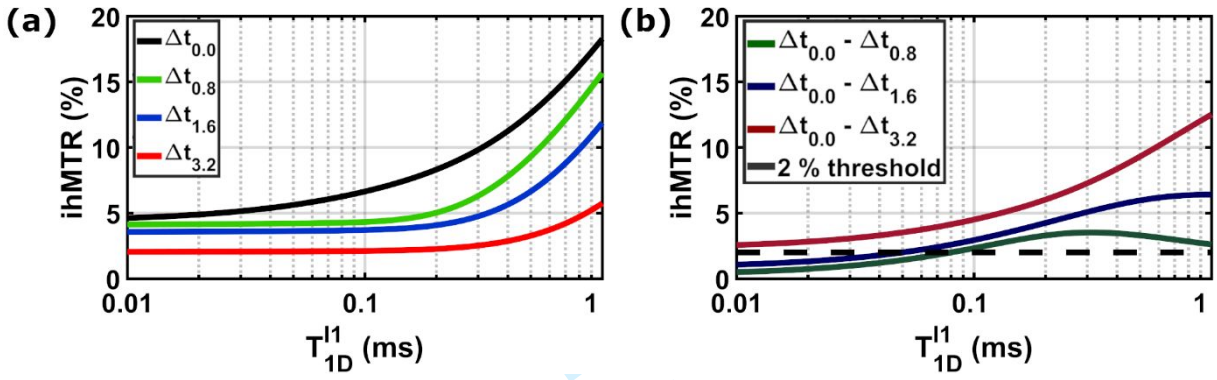

Figure S2: The evolution of MT^{+} and $MT^{\pm}$ as a function of T_{1D}^{I1} for the bi-T_{1D} model and WM tissue parameters. Increasing Δt leads to a less efficient $MT^{\pm}$ saturation, which approached the MT^{+} curve, resulting besides the natural filtering of short T_{1D} components into a supplementary filtering of long T_{1D} components. T_{1D}^{I2} is fixed at 6 ms, while T_{1D}^{I1} is varied in the [10 µs; 1ms] range.

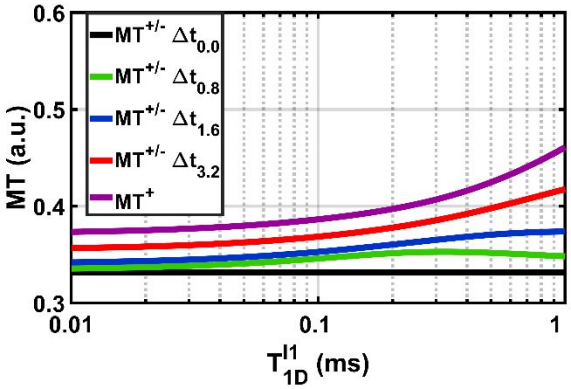

Figure S3: The variation of the high-pass $\Delta t_{3.2}$ T_{1D}-filter shape with varying model parameters.

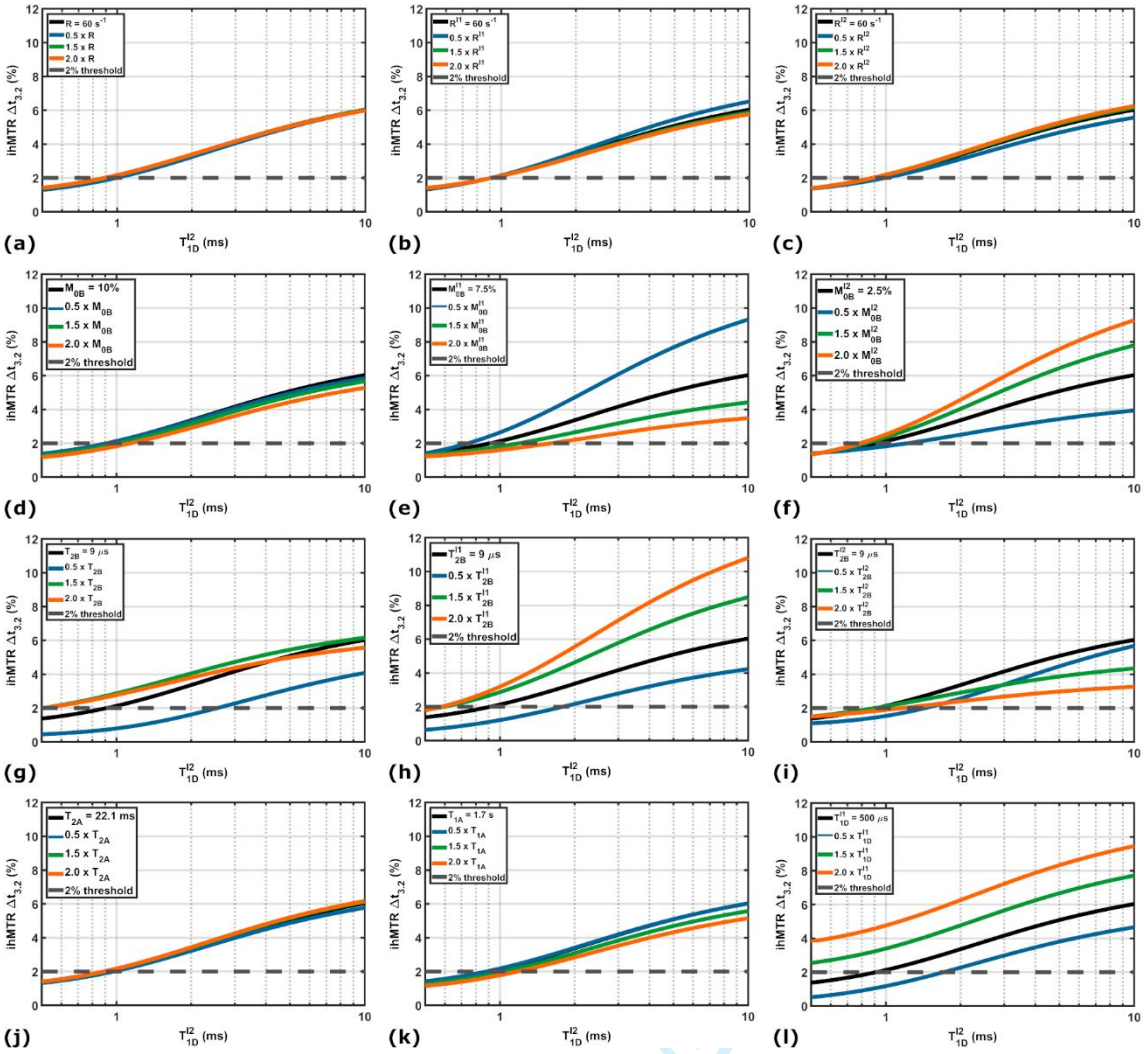
(a)
(b)
(c)
(d)
(e)
(f)
(g)
(h)
(i)
(j)
(k)
(l)
ihMTR Δt3,2 (%)
T1D^I2 (ms)
2% threshold

Figure S4: The variation of the band-pass $\Delta t_{0.0} - \Delta t_{0.8}$ T_{1D}-filter shape with varying model parameters.